

Helicity oscillations in Rayleigh-Bénard convection of liquid metal in a cell with aspect ratio 0.5

Rahul Mitra,¹ Frank Stefani,¹ Vladimir Galindo,¹ Sven Eckert,¹ Max Sieger,¹ Tobias Vogt,¹ and Thomas Wondrak¹

Helmholtz-Zentrum Dresden-Rossendorf, Bautzner Landstr. 400, 01328 Dresden, Germany

(*Electronic mail: f.stefani@hzdr.de)

In this paper, we present numerical and experimental results on helicity oscillations in a liquid-metal Rayleigh-Bénard (RB) convection cell, with an aspect ratio of 0.5. We find that helicity oscillations occur during transitions of flow states that are characterised by significant changes in the Reynolds number. Moreover, we also observe helicity oscillations at flow conditions where the temporal gradient of the change in the Reynolds number is significantly smaller than that of the helicity. Notably, the helicity oscillations observed during the transient double-roll state exhibit characteristics remarkably similar to those associated with the Tayler Instability.

PACS numbers: 47.20.-k 52.30.Cv 47.35.Tv

Keywords: [Rayleigh-Bénard convection](#), [helicity](#), [liquid metal flow](#).

I. INTRODUCTION

Rayleigh-Bénard (RB) convection is a key paradigm of fluid dynamics. A fluid volume (with height H and diameter D) that is heated at the bottom and cooled at the top acquires a temperature difference that leads to a motion of the fluid. Depending on the aspect ratio ($\Gamma = D/H$), this motion can, for instance, take on the form of a flywheel structure with one or multiple stacked roll(s)¹⁻³ or that of a jump rope vortex^{4,5}. In either case, it is the scaling of the Nusselt (Nu) and the Reynolds number (Re) with the Rayleigh (Ra) and the Prandtl number (Pr) of the liquid which is of highest relevance. Grossmann and Lohse⁶ had set-up a systematic theory for those scalings, distinguishing four regimes (with some subdivisions) in the parameter space of Ra and Pr , defined by whether the boundary layer or the bulk dominates the global kinetic and thermal dissipation. In this context, liquid metal experiments are particularly suited to explore the region of low Prandtl numbers in the universal Grossmann-Lohse phase diagram. Pertinent experiments were carried out with mercury^{1,7-9}, pure gallium^{4,10}, the eutectic alloy GaInSn^{2,5,11-13}, and sodium¹⁴. For aspect ratio $\Gamma = 1$, the experiments by Ren et al.¹³ revealed a scaling of $Nu \sim Ra^{0.25}$, in correspondence with the predictions of the Grossmann-Lohse theory for their so-called I_I regime. By contrast, convection in a more slender cylinder with $\Gamma = 0.5$ shows a modified scaling $Nu \sim Ra^{0.288,11,12}$. In this geometry the resulting turbulent flow is characterized by chaotic transitions between single, double and triple rolls, as was recently revealed by employing Contactless Inductive Flow Tomography (CIFT) for reconstructing the global 3D flow field^{15,16}.

A second aspect of liquid metal experiments¹⁷⁻²¹ is their intricate connection to magnetohydrodynamics. In a recent "pub crawl" through the parameter space, using the RoMag device at the University of California, the interplay between convective, magnetic, and rotational forces was explored in much detail^{22,23}. However, the impact of magnetic fields on convection reflects only one direction of magnetohydrodynamic interactions. Conversely, convection is also considered an essential ingredient of magnetic field generation in planets and

stars via hydromagnetic dynamo action^{24,25}.

A decisive role in this process is played by the helicity of the flow²⁶, i.e. the scalar product of the velocity and vorticity, which is capable of inducing electrical currents *in the direction* of a prevailing magnetic field. This so-called α -effect represents a key ingredient of α^2 -dynamos, such as the geodynamo, as well as of $\alpha - \Omega$ -dynamos, such as the solar dynamo. While for a long time the focus of dynamo theory was mainly on a constant α -effect, the interest has recently shifted to the role of its temporal variations. For an early treatment of an oscillatory α -effect in the context of the solar dynamo, see the work by Bushby and Proctor²⁷.

Returning to convection, it is quite obvious that the sloshing motion of Large-Scale Circulation (LSC), with its oscillating sidewise deflection of the single-roll "flywheel", is connected with a corresponding helicity oscillation. A similar helicity oscillation was also observed in simulations of the current-driven, kink-type Tayler Instability (TI), first for the simple case of a full, non-rotating cylinder²⁸, but later also for a quite realistic model of a rotating star²⁹. Remarkably, in either case the helicity oscillation of the dominant flow mode with its azimuthal wavenumber $m = 1$ goes along with a negligible change of the energy content of the flow.

This observation has motivated recent modelling efforts to explain the amazing synchronicity of the solar Schwabe cycle with the 11.07-year alignment cycle of the tidally-dominant planets, Venus, Earth and Jupiter, in terms of an energy-efficient tidal entrainment mechanism for the helicity at the solar tachocline³⁰⁻³⁶. In this context one may ask whether tidal helicity synchronization can be observed in the laboratory. In view of the significant technical challenges to perform TI experiments with liquid metals³⁷, a first attempt to study this effect in the lab was made on the basis of a classical RB-flow in a $\Gamma = 1$ cylinder, exposed to a tide-like ($m = 2$) force exerted by two oppositely situated coils^{38,39}. At a critical strength of the "tidal" force, synchronization of the helicity of the flow was indeed observed (although in a spatially segregated manner).

But what about helicity, and its potential synchronization, in RB-flows with $\Gamma < 1$, which are typically characterized by

transitions between single, double and triple rolls¹⁶? Leaving the synchronization issue to future work, this paper is primarily concerned with the time evolution of the helicity in $\Gamma = 0.5$ convection, its specification for single, double and triple rolls, and the transitions between them.

We will start with numerical simulations for $Ra = 1.8 \times 10^7$ for which we will characterize in detail helicity reversals (i.e., half oscillations) for the two cases of a single vortex flow and a double vortex flow. Informed by that, we will go over to an experiment carried out at the much higher Rayleigh number $Ra = 6.02 \times 10^8$, for which we will determine the 3D flow by CIFT. After shortly recalling the experimental set-up of the $\Gamma = 0.5$ experiment¹⁶, we will analyse exemplary helicity reversals of the experimental flow.

II. SIMULATION

A. Simulation setup

The flow in a RB cell of height 640 mm and diameter 320 mm was directly simulated (without any turbulence modelling) for more than 6 h using the pisoFOAM solver of the finite volume library OpenFOAM. For the simulations a very fine mesh consisting of 1563028 cells was used. In order to cover a long period with a reasonable numerical effort and calculation time, the temperature difference was limited to 0.2 K, which is equivalent to a Rayleigh number $Ra = 1.8 \times 10^7$. Subsequently, the very finely discretized OpenFOAM velocities were interpolated on a coarser cylindrical mesh, containing 5760 linear hexahedral elements with a constant edge length of 25 mm over the height and a mean edge length of 20 mm over the diameter, with a total of $n_{vol} = 6625$ discretized points. These interpolated velocity fields then served for further analysis, in particular for comparisons with respective CIFT results. They were stored at every second, and for our analysis we considered the time period from 8000 s to 21600 s when the convective flow was safely established.

B. General flow characteristics

The typical time scale to characterize the dynamics of an LSC is the free-fall time t_{ff} , i.e. the time taken for a hot plume to rise from bottom to top according to the density difference which, in turn, depends on the temperature difference:

$$t_{ff} = \sqrt{\frac{H}{g\alpha\Delta T}}. \quad (1)$$

Here, g is the acceleration due to gravity, H is the height of the cell, α is the coefficient of volume expansion, and ΔT is the temperature difference between top and bottom plate. For our specific simulation, the free-fall time is 51.4 s.

The global, volume averaged Reynolds number of the flow was calculated using the following expression:

$$Re_{vol} = \frac{\bar{v}H}{\nu}, \quad (2)$$

where \bar{v} is the volume averaged flow velocity, and ν is the kinematic viscosity.

The mean helicity density of the flow was calculated using the following expression:

$$h = \frac{\sum_{i=1}^{n_{vol}} w_i (\mathbf{v}_i \cdot (\nabla \times \mathbf{v}_i))}{\sum_{i=1}^{n_{vol}} w_i}, \quad (3)$$

where w_i is the volume associated with each element of the coarser cylindrical grid, \mathbf{v}_i is the velocity in this element i , and $\nabla \times \mathbf{v}_i$ is the vorticity therein. As a density of helicity, h has the dimension $[LT^{-2}]$ and will always be given in units $\text{mm}^2 \text{s}^{-2}$. Henceforth, we will frequently use the term "helicity" for the "mean helicity density", although the former would, strictly speaking, be the volume integral over the local helicity density.

In order to get a preliminary overview about the flow modes that typically appear in our problem, we have carried out a proper orthogonal decomposition (POD), similar to the formulation described by Wondrak et al.¹⁶. The first 8 POD

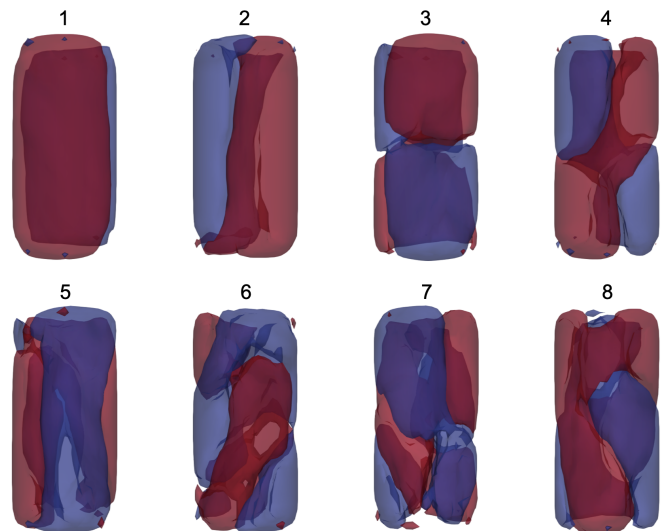


FIG. 1: The first 8 POD modes extracted from the simulated velocity field: 3D isosurfaces of the vertical velocity referred to a value corresponding to ± 0.1 of the respective maximum value.

modes are shown in Fig. 1. Modes 1 and 2 resemble a single roll state (SRS), while modes 3 and 4 resemble a double roll state (DRS). Mode 6, in turn, is a twisted structure, dominated by three rolls over the height, which will therefore be called triple roll state (TRS). The rest of the modes 5, 7 and 8 represent other structures which cannot easily be classified as a SRS, DRS or a TRS. Modes above 8 contribute to less than 2% of the total energy. The individual energy contributions of the SRS, DRS and TRS were calculated over time.

C. Time evolution

The global Reynolds number Re_{vol} and the mean helicity density h over a representative time interval of 100 free-

fall times from the entire simulation are shown in Fig. 2(a). While the Reynolds number fluctuates only moderately be-

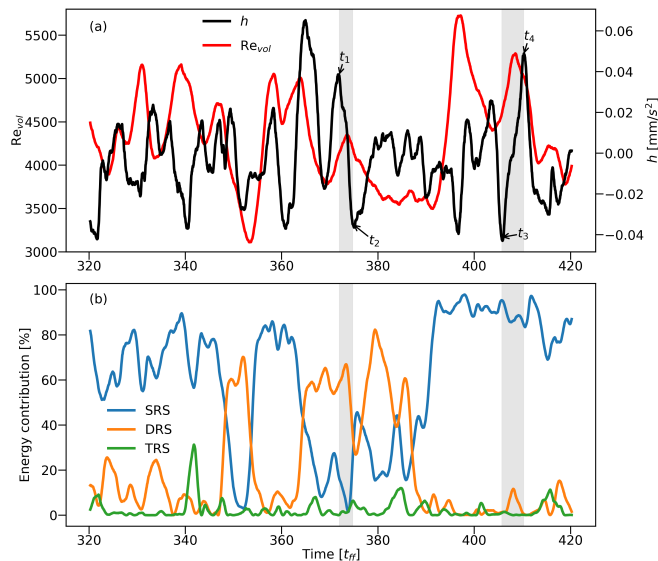


FIG. 2: (a) Global Reynolds number (red) and mean helicity density (black) over time of the simulated velocity field. (b) Energy contributions of SRS (blue), DRS (orange), TRS (green) to the overall flow structure. The time is given in units of t_{ff} . Two exemplary helicity reversals are shaded in grey, between $t_1 - t_2$ and $t_3 - t_4$.

tween values of 3100 and 5600, the mean helicity density fluctuates strongly, acquiring both positive and negative values with amplitudes of up to 0.06 mms^{-2} . Quite often one observes concurrent changes of Reynolds number and helicity which, on closer inspection, correspond to transitions between flow modes with different roll numbers.

However, there are also periods where the helicity fluctuates significantly, while the flow structure remains relatively stable and the rate of change of the Reynolds number is quite small. Two such time intervals are marked in Fig. 2(a), where between $t_1 - t_2$ ($\approx 2.8 t_{ff}$) and $t_3 - t_4$ ($\approx 4.6 t_{ff}$) the mean helicity density changes its sign, while the Reynolds number is quite stable. Before analyzing those intervals in more detail, we show in Fig. 2(b) the energy contributions of the individual flow modes over time.

Quite generally, the SRS, represented in blue, is the most dominant mode, often reaching more than 80% of the total energy. The pattern of fluctuation does not appear to be periodic, being an indication for, in general, chaotic dynamics of the flow. The DRS, shown in orange, also exhibits fluctuations, but with a generally lower percentage of the total energy compared to the SRS. The energy level of the DRS fluctuates between 20% and 60%. The TRS, depicted in green, contributes the least energy among the three states, with most values remaining below 20%. The strong changes in the energy shares occurring at certain times are a symptom of the transformation between the different flow states. In Appendix A, we will discuss the dominant frequencies of those variations.

D. Helicity reversals

Helicity in fluid dynamics refers to the "handedness", or chirality, of the flow structure, which can be understood as the direction in which the flow twists or spirals. A reversal of helicity implies that a flow structure that was twisting in one direction is now twisting in the opposite direction.

In the following, we will discuss those helicity reversals (i.e., half oscillations) that take place within a time interval when the dominant type of flow mode mainly persists. Since we have not observed any long enough interval with a dominant TRS, we will focus exclusively on the SRS and DRS. We start with the latter, for which we detail in Fig. 3 the helicity evolution between $t_1 - t_2$ (cp. Fig. 2(a)). As it is obvious from Fig. 3(a), the mean helicity density reversal comes about *without* any significant change in the Reynolds number (just around 5%) which indicates that the flow maintains its overall energy. It is also seen in Fig. 3(b) that the DRS is dominant until the end of the interval when the SRS starts to gain comparable strength.

Similarly as in the work by Jüstel et al.³⁹, we distinguish here between the vertical and the horizontal contributions of the mean helicity density, h_z and h_{hor} , which result from $v_z \cdot (\nabla \times \mathbf{v})_z$ and $v_x \cdot (\nabla \times \mathbf{v})_x + v_y \cdot (\nabla \times \mathbf{v})_y$, respectively. In our problem, h_{hor} represents mainly the sloshing motion of the LSC, characterized by a side-wise deflection of the large-scale roll with its dominant horizontal vorticity. h_z , in turn, corresponds to some torsional motion where the large-scale roll is tilted and thereby acquires a vertical vorticity component $(\nabla \times \mathbf{v})_z$ (some corresponding vertical motion is then still required to produce a non-zero h_z).

As can be seen in Fig. 3(c), these two contributions evolve similarly, although the amplitude of h_{hor} is about two times larger than h_z . Still more details can be observed in Fig. 3(d), where we further distinguish between the values of h_{hor} and h_z in the top and in the bottom half of the cylinder. Basically, h_z and h_{hor} show a quite comparable behaviour in the two halves, meaning that there is no significant cancellation going on. The streamlines in Fig. 4, color-coded by the vertical velocity component, show the direction of flow and regions of upward (red) and downward (blue) motion for the five particular instants indicated by vertical lines in Fig. 3. Let us start with the flow structure at t_1 . Near mid-height of the cell, the red streamlines, indicative of upward flow, are positioned behind the blue streamlines, which represent a downward flow. As time advances, the red and blue streamlines change their relative positions. By t_2 , the red streamlines near mid-height have moved to the front, a reversal from their original position at t_1 , which indicates that the flow now has an opposite helicity compared to the initial state. The helicity reversal of the DRS resembles the chirality reversal reported by Weber et al.²⁸ for the case of the kink-type, current-driven TI. However, the flow structure at t_2 is not perfectly mirror-symmetric to that at t_1 , since the SRS has already gained some comparable strength.

The helicity reversal for an SRS, documented in Figs. 5 and 6, is a bit different from the case of the twisted DRS. As seen in Fig. 5(c), the two contributions h_{hor} and h_z evolve quite in parallel with nearly identical contributions. The same applies

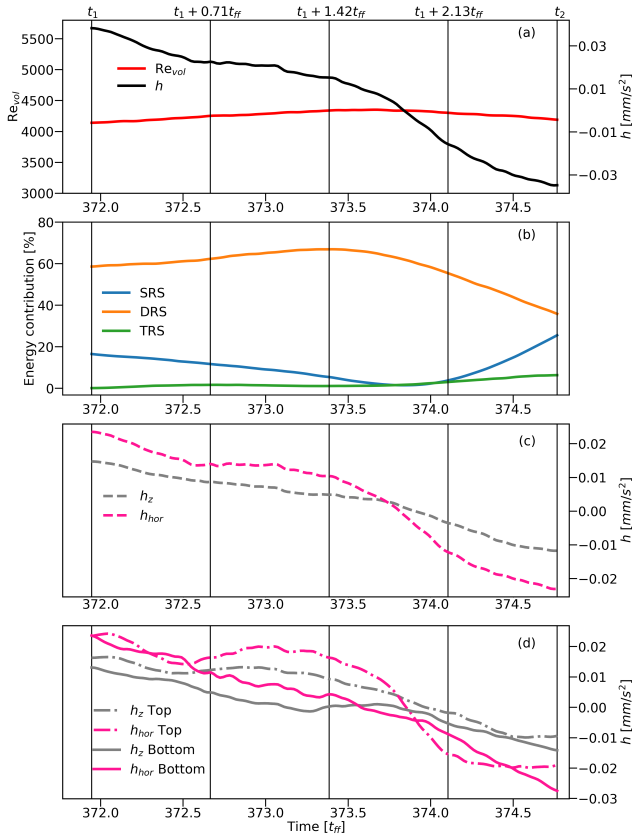


FIG. 3: (a) Global Reynolds number (red) and mean helicity density (black); (b) Energy contributions of SRS (blue), DRS (orange), TRS (green); (c) Vertical (dashed grey) and horizontal components of the mean helicity density (dashed pink); (d) Vertical (grey) and horizontal (pink) components of the mean helicity density at top half of the cylinder (dash-dotted) and bottom half of the cylinder (solid), within the time interval t_1 to t_2 of the simulated flow.

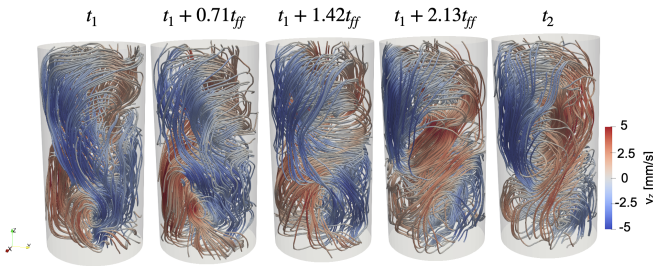


FIG. 4: Illustration of the helicity reversal at nearly constant Reynolds number for a DRS, within the time interval t_1 to t_2 of the simulated flow. The snapshots correspond to the five instants indicated by vertical lines in Fig. 3.

to their shares in the two half-spaces (Fig. 5(d)), apart from an interesting detail between 407 and $408 t_{ff}$ where the helicities in the two half spaces seem to evolve contrary, thereby compensating each other to some extent.

Fig. 6 shows that in case of an SRS, the large-scale "fly-

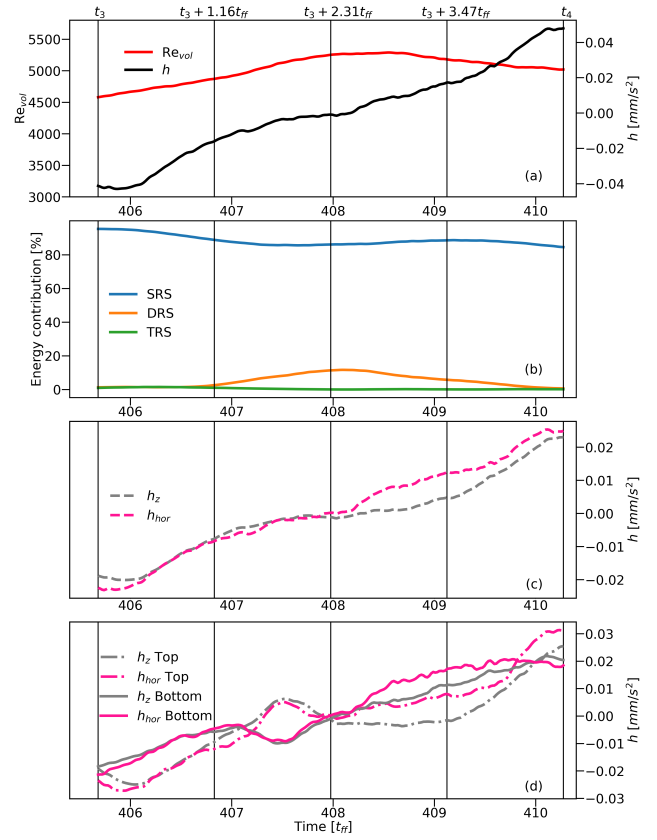


FIG. 5: (a) Global Reynolds number (red) and mean helicity density (black); (b) Energy contributions of SRS (blue), DRS (orange), TRS (green); (c) Vertical (dashed grey) and horizontal components of the mean helicity density (dashed pink); (d) Vertical (grey) and horizontal (pink) components of the mean helicity density at top half of the cylinder (dash-dotted) and bottom half of the cylinder (solid), within the time interval t_3 to t_4 of the simulated flow.

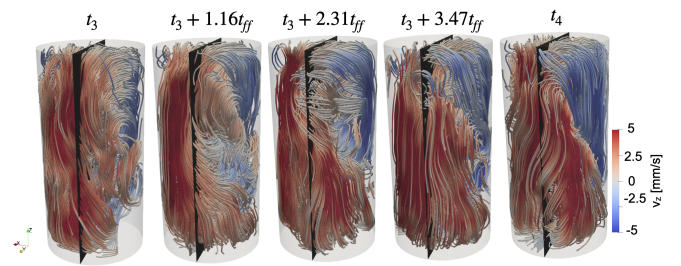


FIG. 6: Illustration of the helicity reversal at nearly constant Reynolds number for a SRS, within the time interval t_3 to t_4 of the simulated flow. The snapshots correspond to the five instants indicated by vertical lines in Fig. 5.

wheel" undergoes sloshing from left to right, whereby the main hot and cold plumes move horizontally over time. It is also important to note that the time taken for the helicity reversal in case of the SRS is longer than the respective reversal for twisted DRS. This is in agreement with the Fourier

spectral analysis of the helicity and the energy contributions of the SRS and DRS, where the high frequency peaks of helicity are dominated relatively more by the DRS as compared to the SRS (see Appendix A).

III. EXPERIMENT

A. Experimental setup

This section begins with a short sketch of the experimental set-up, more details of which can be found in the work of Wondrak et al.¹⁶ The RB experimental system is shown in Fig. 7. The cell with a height of 640 mm and a diameter of 320 mm is filled with the ternary alloy GaInSn, a liquid metal with an eutectic temperature of 10.5 °C. In the experiment, the Prandtl number is $Pr = 0.031$. In order to ensure adiabatic boundary conditions in radial direction, the cell is encapsulated in styrofoam insulation. It has two copper heat exchangers, one at the top and the other at the bottom, to achieve nearly constant temperature boundary conditions in axial direction. For the realization of the CIFT measurements, four circular excitation coils generate a magnetic field in the axial direction, and two rectangular coils generate a magnetic field in the horizontal direction. However, for our experiment, we followed the *one-*

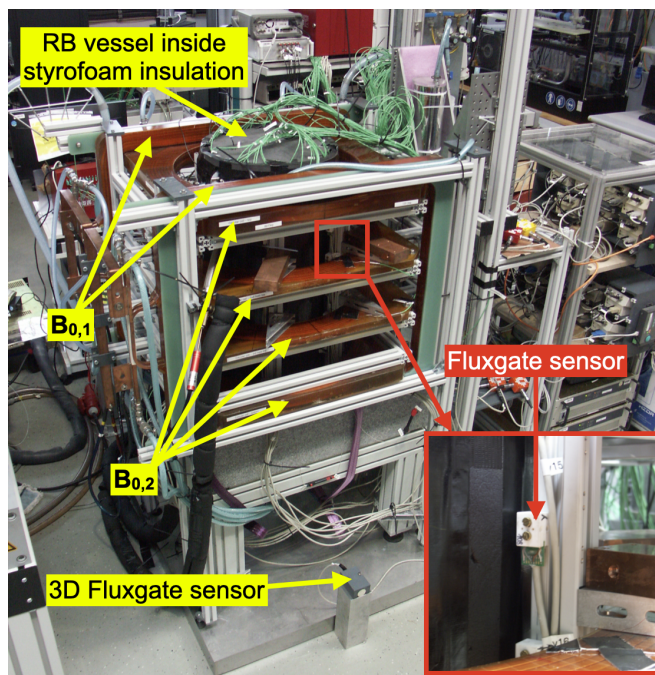


FIG. 7: The RB experimental system with the CIFT measurement system⁴⁰.

field excitation scheme, described by Mitra et al.⁴⁰, utilizing only the axial field, which is largely sufficient to reconstruct the dominant flow structures. The radial components of the induced magnetic fields were recorded by 42 fluxgate sensors arranged in a 7×6 (height × azimuth) configuration around the side walls of the cell. These sets of magnetic fields mea-

sured at every second were used to reconstruct the 3D velocity at the corresponding time instances by solving a linear inverse problem^{15,41–44}, using the fast reconstruction algorithm to speed up the regularization procedure⁴⁵.

The total duration of the experiment was 30000 seconds, with 1 h duration at the beginning when the temperature difference was zero, followed by 6 h of flow driven by a temperature difference of nearly 12 K, corresponding to a Rayleigh number of $Ra = 6.02 \times 10^8$, and then again the temperature difference was brought down to zero, quickly terminating the flow.

B. General flow characteristics

The free-fall time for the experimental flow, using the definition from Eqn. 1, is 8.9 s. As CIFT is known to provide only a global picture of the flow while smoothing out fine structures, we have examined in Appendix B how reliable it is in reconstructing the helicity of the flow. For that purpose we have used the numerically simulated flow field from which we generated a synthetic CIFT reconstruction. As shown in Appendix B, CIFT is in general well capable of extracting the helicity fluctuations of the original flow, though with the typical underestimation of the amplitudes due to the smoothing effect.

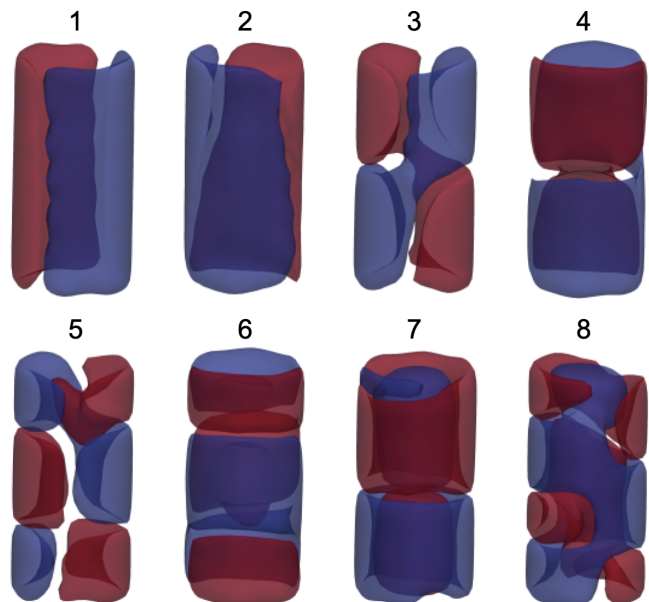


FIG. 8: The first 8 POD modes extracted for the CIFT-reconstructed experimental velocity field¹⁶: 3D isosurfaces of the vertical velocity referred to a value corresponding to ± 0.1 of the respective maximum value.

Similar to the case of simulations, the first 8 POD modes of the experimental flow, as extracted from CIFT, are shown in Fig. 8. Here, modes 1 and 2 were grouped as SRS, modes 3 and 4 were categorized as DRS and modes 5 and 6 were classified as TRS. Modes 7 and 8 exhibit torus-shaped flow states,

which have resemblances to a DRS and a TRS, respectively. Vertical upward and downward movements are still seen on the sidewall, but the recirculation of fluid closes in the center zone around the axis of the cylinder.

C. Time evolution

The global Reynolds number and the mean helicity density for the entire duration of the experiment are shown in Fig. 9. During the first hour, the Reynolds number (as well as

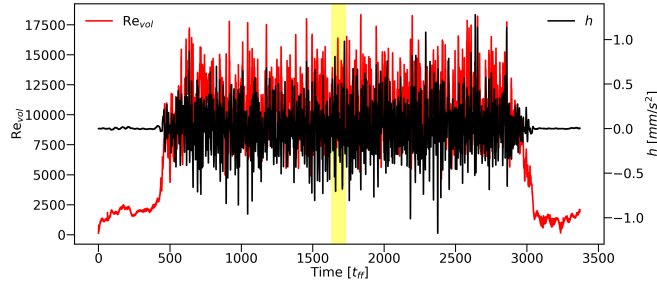


FIG. 9: Global Reynolds number (red) and mean helicity density (black) for the entire duration of the experiment with the 100 free-fall duration shaded in yellow.

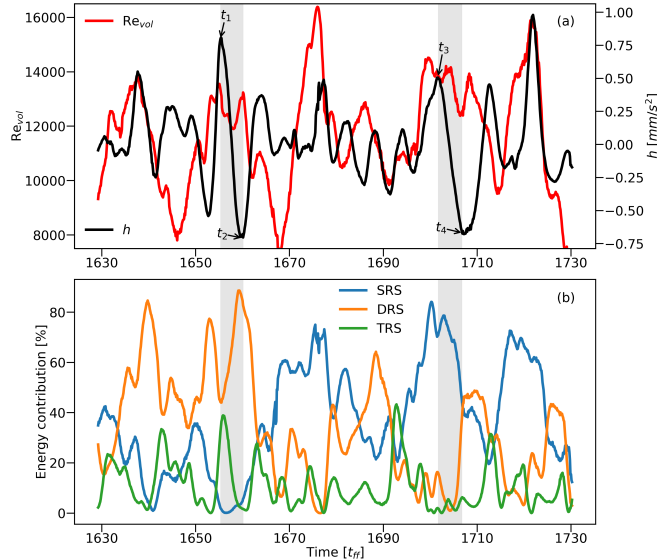


FIG. 10: (a) Global Reynolds number (red) and mean helicity density (black). (b) Energy contributions of SRS (blue), DRS (orange), TRS (green) to the overall flow structure for 15 min (100 free-fall time units) of flow (shaded in yellow in Fig. 9). Two exemplary helicity reversals are shaded in grey, between $t_1 - t_2$ and $t_3 - t_4$.

the mean helicity density) of the flow remained nearly zero. Upon setting the temperature difference between top and bottom, both mean helicity density and Reynolds number began to rise and fluctuate, signaling the onset of fluid motion and the development of a turbulent flow.

For the restricted time interval, marked by the yellow area in Fig. 9, Fig. 10(a) shows the global Reynolds number and the helicity over time. Correspondingly, in Fig. 10(b) we plot the dominant contributions to the flow. Just as in the simulations discussed above, the three flow states exhibit distinct behaviors over time, with the SRS modes being the most energetic and dynamic, followed by the DRS modes, and with the TRS modes being the least energetic.

D. Helicity reversals

Helicity reversals in case of dominating DRS and SRS were also observed in the experiment. The corresponding time intervals t_1 to t_2 (Fig. 11) and t_3 to t_4 (Fig. 13) have been marked by black arrows in Fig. 10. The time interval between t_2 and t_1 is approximately $4.8 t_{ff}$, whereas the interval between t_4 and t_3 is around $5.1 t_{ff}$. Figs. 12 and 14 visualize the corresponding 3D velocity fields for the two specified time intervals.

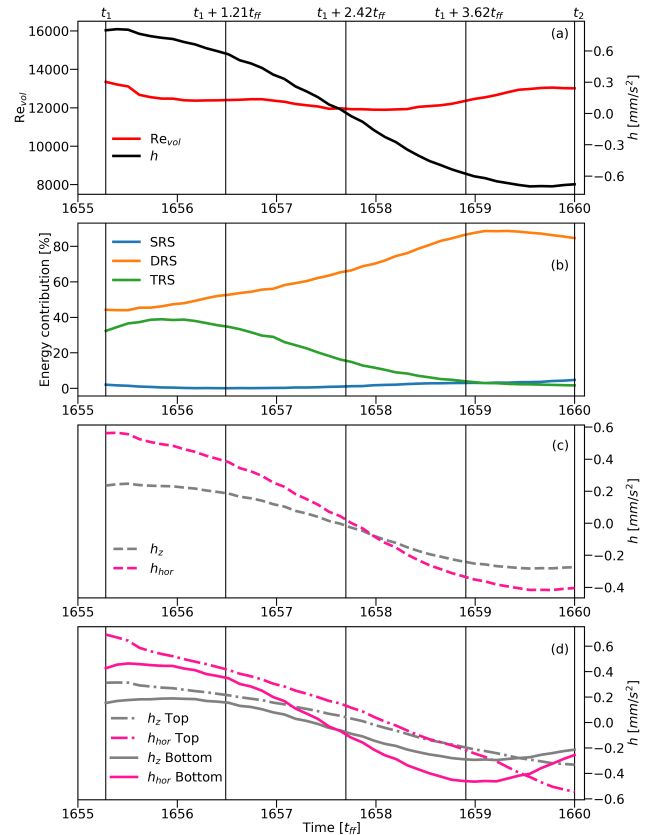


FIG. 11: (a) Global Reynolds number (red) and mean helicity density (black); (b) Energy contributions of SRS (blue), DRS (orange), TRS (green); (c) Vertical (dashed grey) and horizontal components of the mean helicity density (dashed pink); (d) Vertical (grey) and horizontal (pink) components of the mean helicity density at top half of the cylinder (dash-dotted) and bottom half of the cylinder (solid), within the time interval t_1 to t_2 of the experimental flow.

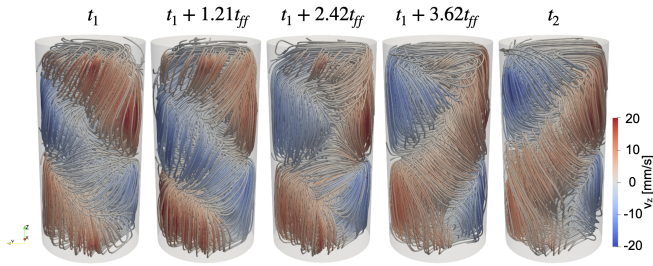


FIG. 12: Illustration of the helicity reversal at nearly constant Reynolds number for a DRS, within the time interval t_1 to t_2 of the experimental flow. The snapshots correspond to the five instants indicated by vertical lines in Fig. 11.

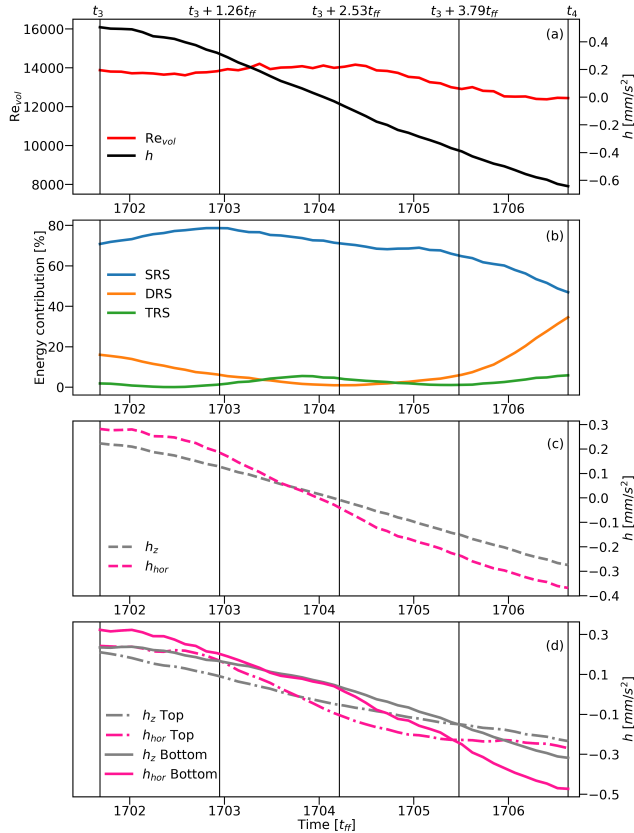


FIG. 13: (a) Global Reynolds number (red) and mean helicity density (black); (b) Energy contributions of SRS (blue), DRS (orange), TRS (green); (c) Vertical (dashed grey) and horizontal components of the mean helicity density (dashed pink); (d) Vertical (grey) and horizontal (pink) components of the mean helicity density at top half of the cylinder (dash-dotted) and bottom half of the cylinder (solid), within the time interval t_3 to t_4 of the experimental flow.

Quite generally, the experimentally observed features are very similar to those of the simulated flow. For the DRS, the horizontal component of the mean helicity density, h_{hor} , is significantly stronger than the vertical one, h_z (Fig. 11(c)), while their respective evolutions in the top and bottom half spaces

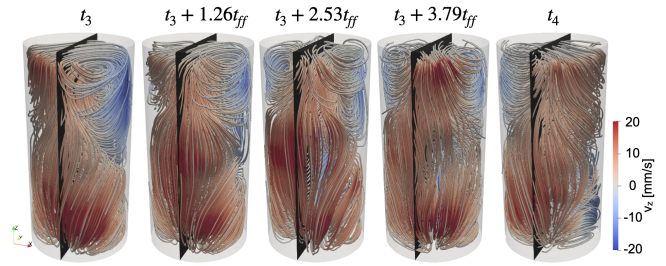


FIG. 14: Illustration of the helicity reversal at nearly constant Reynolds number for a SRS, within the time interval t_3 to t_4 of the experimental flow. The snapshots correspond to the five instants indicated by vertical lines in Fig. 13.

(Fig. 11(d)) are quite parallel. The change of twist in Fig. 12 is more evident than in the case of simulations (Fig. 4), which might have to do with the "contamination" of the DRS by SRS at the end of the considered interval as discussed above.

As for the SRS, Fig. 13(c) shows again that h_{hor} and h_z evolve very similarly, with only a slight preponderance of h_{hor} . Also the evolutions in the top and bottom halves proceed in parallel (Fig. 13(d)), quite consistently with the simulation results from Fig. 5(d). Again, the sloshing motion illustrated in the five snapshots of Fig. 14 appears somewhat smoother than the corresponding simulation results of Fig. 6.

IV. CONCLUSION

In this study, we have analyzed the flow evolution in a slender RB convection cell which is characterized by frequent and chaotic transitions between SRS, DRS and TRS. Using both numerical simulations and experimental results, our main focus was on the relation between those specific flow modes and the helicity of the flow. Apart from concurrent changes of flow modes and helicity, we also observed helicity reversals within a given flow mode when the Reynolds number is nearly constant.

For the SRS, the helicity reversal goes along with a clearly visible sloshing motion of the elongated "flywheel". Yet, in addition to its corresponding horizontal part, the reversing helicity contains also an equally strong vertical part, pointing to a torsional component of the flow. A full period of these changes (i.e., the double of the observed reversal times) is in the range of 8 free-fall times, in good agreement with previous results of Wondrak et al.¹⁶ In any case, the helicity parts in the top and bottom half of the cylinder behave similarly.

For the DRS, the helicity reversals, which correspond to a simultaneous twisting of the two flow cells which are stacked over each other, proceed a bit faster than in case of the SRS. The horizontal contribution of the helicity is typically stronger than the vertical one. As in the SRS case, the evolutions in the top and bottom halves are in phase. Remarkably, the flow and helicity evolution in this DRS case is very similar to that in case of the kink-type, current-driven TI, as previously observed by Weber et al.²⁸ (see, in particular, the animated version of Fig. 13, available in the supplementary material of

that paper). Hence, whatever the specific driving agent of the DRS might ever be, its helicity evolution turns out to be a quite generic and universal feature.

Investigations of potential tidal synchronization for the slender RB cell, as previously carried out for the $\Gamma = 1$ cell³⁹, are planned for the future. The same applies to the corresponding helicity evolution for flows with $\Gamma \gg 1$ which might indeed be of high relevance for the so-called small-scale dynamo in the shallow subsurface layer of the Sun⁴⁶.

ACKNOWLEDGMENTS

The authors would like to express their gratitude to Thomas Gundrum and Stefanie Sonntag for their invaluable technical support throughout the course of the experiment. Additionally, R.M. would like to extend their appreciation to Ashish Mishra for engaging in insightful discussions that enriched the research.

FUNDING

This work is supported by the Deutsche Forschungsgemeinschaft (DFG) under the grant VO 2331/1.

CONFLICT OF INTEREST

The authors have no conflicts to disclose.

DATA AVAILABILITY STATEMENT

The data that support the findings of this study are available from the corresponding author upon reasonable request.

AUTHOR CONTRIBUTIONS

Rahul Mitra: Conceptualization (support), Data curation (lead), Formal analysis (lead), Investigation (lead), Methodology (support), Software (equal), Visualization (lead), Writing - original draft (equal), Writing - review & editing (equal) **Frank Stefani:** Conceptualization (lead), Methodology (lead), Project administration, Supervision (lead), Visualization (support), Writing - original draft (equal), Writing - review & editing (equal) **Vladimir Galindo:** Software (equal), Writing - review & editing (equal) **Sven Eckert:** Supervision (support), Writing - review & editing (equal) **Max Sieger:** Investigation (equal), Supervision (support), Writing - review & editing (equal) **Tobias Vogt:** Funding acquisition (lead), Supervision (support), Writing - review & editing (equal) **Thomas Wondrak:** Methodology (support), Supervision (support), Writing - review & editing (equal) All authors have read and agreed to the published version of the manuscript.

Appendix A: Fourier spectra of simulation data

A Fourier spectral analysis was performed to discern the time-dependence of the helicity, the Reynolds number, and the energy contributions of single, double, and triple roll states within the turbulent flow. The Fourier spectra of the mean helicity density, Reynolds number and the energy contributions of the flow states are shown in Fig. 15.

The first observation concerns a very prominent peak at 2.46 mHz (corresponding to nearly $8 t_{ff}$) observed in the helicity spectrum which signifies a substantial periodic contribution to the helicity of the flow. Looking back on Figs. 5 and 6 (where the period of half an oscillation was $4.6 t_{ff}$) it appears that this period is quite representative for a typical helicity oscillation within an SRS. Notably, such a period is also consistent with the work of Wondrak et al.¹⁶ where a typical change rate of the LSC's angle of 40° - $50^\circ/t_{ff}$ had been observed (see page 23 of that paper).

By contrast, the observed period for the DRS case (see Figs. 5 and 6) was $5.7 t_{ff}$, corresponding to 3.4 mHz. A secondary peak close to this value is visible in Fig. 15(a).

At any rate, the typical peaks for the Reynolds number in Fig. 15(b) are at significantly lower frequencies than those for the helicity. One of those peaks, at 1.7 mHz, shows also up in

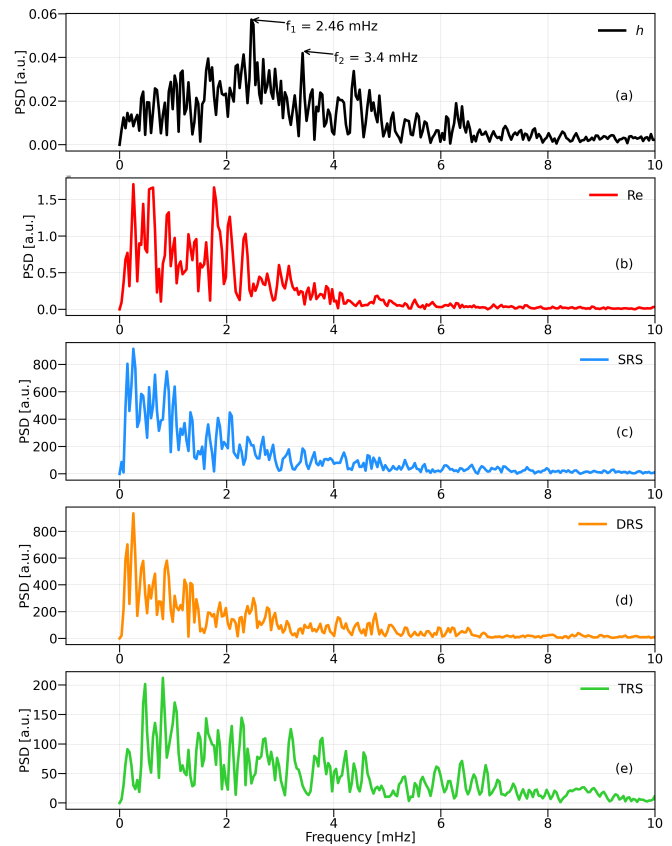


FIG. 15: Fourier spectra of (a) helicity (black), (b) Reynolds number (red), energy contribution of (c) SRS (blue), (d) DRS (orange) and (e) TRS (green) for the simulation.

the spectrum of the SRS energy (Fig. 15(c)) which indicates that the spectrum of the Reynolds number is dominated by the transitions of different flow types. This is confirmed by a closer inspection of the typical transition times between the flow modes in Fig. 2(b).

Appendix B: Helicity comparison

To investigate the reliability of CIFT for reconstructing the helicity of the flow, we have used the simulated velocity field (see section II), from which we generated a synthetic CIFT reconstruction with the same excitation magnetic field and sensor arrangement as used in the experiment (see section III A). The mean helicity density of the simulated flow can then be compared to that of the flow reconstructed by CIFT.

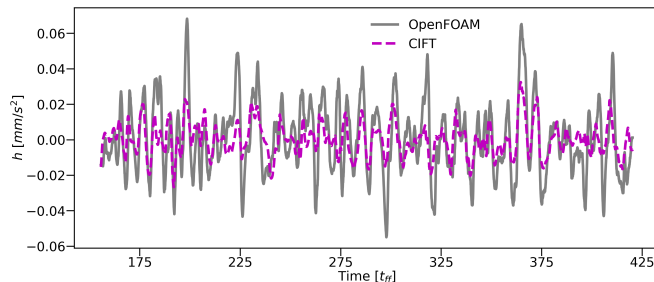


FIG. 16: Time-dependent mean helicity density of the simulated velocity field (solid, grey) and of the corresponding CIFT-reconstructed field (dashed, magenta).

Fig. 16 illustrates the time variation of the mean helicity density of the simulated (solid, grey) and the reconstructed flow (dashed, magenta), over the 13 600 s of chosen simulation time. The general variations are appreciably reconstructed by CIFT. The mean correlation is 66.4%, which is in accordance with the mean quality of reconstruction for this particular sensor configuration and excitation scheme⁴⁰.

- ¹S. Cioni, S. Cilberto, and J. Sommeria, “Strongly turbulent Rayleigh–Bénard convection in mercury: comparison with results at moderate Prandtl number,” *J. Fluid Mech.* **335**, 111–140 (1997).
- ²T. Zürner, F. Schindler, T. Vogt, S. Eckert, and J. Schumacher, “Combined measurement of velocity and temperature in liquid metal convection,” *J. Fluid Mech.* **876**, 1108–1128 (2019).
- ³L. Zvirner, A. Tilgner, and O. Shishkina, “Elliptical Instability and multiple-roll flow modes of the large-scale circulation in confined turbulent Rayleigh–Bénard convection,” *Phys. Rev. Lett.* **125**, 054502 (2020).
- ⁴T. Vogt, S. Horn, A. M. Grannan, and J. M. Aurnou, “Jump rope vortex in liquid metal convection,” *Proc. Natl. Acad. Sci.* **115**, 12674–12679 (2018).
- ⁵M. Akashi, T. Yanagisawa, Y. Tasaka, T. Vogt, Y. Murai, and S. Eckert, “Transition from convection rolls to large-scale cellular structures in turbulent Rayleigh–Bénard convection in a liquid metal layer,” *Phys. Rev. Fluids* **4**, 033501 (2019).
- ⁶S. Grossmann and D. Lohse, “Scaling in thermal convection: a unifying theory,” *J. Fluid Mech.* **407**, 27–56 (2000).
- ⁷T. Takeshita, T. Segawa, J. A. Glazier, and M. Sano, “Thermal turbulence in mercury,” *Phys. Rev. Lett.* **76**, 1465–1468 (1996).
- ⁸J. A. Glazier, T. Segawa, A. Naert, and M. Sano, “Evidence against ‘ultrahard’ thermal turbulence at very high Rayleigh numbers,” *Nature* **398**, 307–310 (1999).
- ⁹Y. Tsuji, T. Mizuno, T. Mashiko, and M. Sano, “Mean wind in convective turbulence of mercury,” *Phys. Rev. Lett.* **94**, 034501 (2005).

- ¹⁰E. M. King and J. M. Aurnou, “Turbulent convection in liquid metal with and without rotation,” *Proc. Natl. Acad. Sci.* **110**, 6688–6693 (2013).
- ¹¹F. Schindler, S. Eckert, T. Zürner, J. Schumacher, and T. Vogt, “Collapse of coherent large scale flow in strongly turbulent liquid metal convection,” *Phys. Rev. Lett.* **128**, 164501 (2022).
- ¹²F. Schindler, S. Eckert, T. Zürner, J. Schumacher, and T. Vogt, “Erratum: Collapse of coherent large scale flow in strongly turbulent liquid metal convection [physical review letters 128, 164501 (2022)],” *Phys. Rev. Lett.* **131** (2023), 10.1103/physrevlett.131.159901.
- ¹³L. Ren, X. Tao, L. Zhang, M. J. Ni, K. Q. Xia, and Y. C. Xie, “Flow states and heat transport in liquid metal convection,” *J. Fluid Mech.* **951** (2022), 10.1017/jfm.2022.866.
- ¹⁴R. Khalilov, I. Kolesnichenko, A. Pavlinov, A. Mamykin, A. Shestakov, and P. Frick, “Thermal convection of liquid sodium in inclined cylinders,” *Phys. Rev. Fluids* **3** (2018), 10.1103/physrevfluids.3.043503.
- ¹⁵T. Wondrak, J. Pal, F. Stefani, V. Galindo, and S. Eckert, “Visualization of the global flow structure in a modified Rayleigh–Bénard setup using contactless inductive flow tomography,” *Flow Meas. Instrum.* **21**, 269–290 (2018).
- ¹⁶T. Wondrak, M. Sieger, R. Mitra, F. Schindler, F. Stefani, T. Vogt, and S. Eckert, “Three-dimensional flow structures in turbulent Rayleigh–Bénard convection at low Prandtl number $Pr = 0.03$,” *J. Fluid Mech.* **974**, A48 (2023).
- ¹⁷S. Cioni, S. Chaumat, and J. Sommeria, “Effect of a vertical magnetic field on turbulent Rayleigh–Bénard convection,” *Phys. Rev. E* **62**, R4520–R4523 (2000).
- ¹⁸J. M. Aurnou and P. L. Olson, “Experiments on Rayleigh–Bénard convection, magnetoconvection and rotating magnetoconvection in liquid gallium,” *J. Fluid Mech.* **430**, 283–307 (2001).
- ¹⁹U. Burr and U. Müller, “Rayleigh–Bénard convection in liquid metal layers under the influence of a vertical magnetic field,” *Phys. Fluids* **13**, 3247–3257 (2001).
- ²⁰T. Zürner, F. Schindler, T. Vogt, S. Eckert, and J. Schumacher, “Flow regimes of Rayleigh–Bénard convection in a vertical magnetic field,” *J. Fluid Mech.* **894**, A21 (2020).
- ²¹T. Vogt, J. C. Yang, F. Schindler, and S. Eckert, “Free-fall velocities and heat transport enhancement in liquid metal magneto-convection,” *J. Fluid Mech.* **915**, A68 (2021).
- ²²A. M. Grannan, J. S. Cheng, A. Aggarwal, E. K. Hawkins, Y. Xu, S. Horn, J. Sánchez-Álvarez, and J. M. Aurnou, “Experimental pub crawl from Rayleigh–Bénard to magnetostrophic convection,” *J. Fluid Mech.* **939** (2022), 10.1017/jfm.2022.204.
- ²³J. Schumacher, “The various facets of liquid metal convection,” *J. Fluid Mech.* **946** (2022), 10.1017/jfm.2022.455.
- ²⁴F. Rincon, “Dynamo theories,” *J. Plasma Phys.* **85** (2019), 10.1017/s0022377819000539.
- ²⁵S. M. Tobias, “The turbulent dynamo,” *J. Fluid Mech.* **912** (2021), 10.1017/jfm.2020.1055.
- ²⁶H. K. Moffatt, “Helicity,” *Comptes Rendus Mécanique* **346**, 165–169 (2018).
- ²⁷P. J. Bushby and M. R. E. Proctor, “The influence of α -effect fluctuations and the shear-current effect upon the behaviour of solar mean-field dynamo models,” *Mon. Not. R. Astron. Soc.* **409**, 1611–1618 (2010).
- ²⁸N. Weber, V. Galindo, F. Stefani, and T. Weier, “The Taylor Instability at low magnetic Prandtl numbers: between chiral symmetry breaking and helicity oscillations,” *New J. Phys.* **17**, 113013 (2015).
- ²⁹G. Monteiro, G. Guerrero, F. Del Sordo, A. Bonanno, and P. K. Smolarkiewicz, “Global simulations of Taylor Instability in stellar interiors: a long-time multistage evolution of the magnetic field,” *Mon. Not. R. Astron. Soc.* **521**, 1415–1428 (2023).
- ³⁰F. Stefani, A. Giesecke, N. Weber, and T. Weier, “Synchronized helicity oscillations: A link between planetary tides and the solar cycle?” *Sol. Phys.* **291**, 2197–2212 (2016).
- ³¹F. Stefani, A. Giesecke, N. Weber, and T. Weier, “On the synchronizability of Taylor–Spruit and Babcock–Leighton type dynamos,” *Sol. Phys.* **293** (2018), 10.1007/s11207-017-1232-y.
- ³²F. Stefani, A. Giesecke, and T. Weier, “A model of a tidally synchronized solar dynamo,” *Sol. Phys.* **294** (2019), 10.1007/s11207-019-1447-1.
- ³³F. Stefani, A. Giesecke, M. Seilmayer, R. Stepanov, and T. Weier, “Gleissberg, Suess-de Vries: Towards a consistent model of planetary synchro-

- nization of solar cycles,” *Magnetohydrodynamics* **56**, 269–280 (2020).
- ³⁴F. Stefani, R. Stepanov, and T. Weier, “Shaken and stirred: When Bond meets Suess–de Vries and Gnevyshev–Ohl,” *Sol. Phys.* **296** (2021), [10.1007/s11207-021-01822-4](https://doi.org/10.1007/s11207-021-01822-4).
- ³⁵M. Klevs, F. Stefani, and L. Jouve, “A synchronized two-dimensional α – ω model of the solar dynamo,” *Sol. Phys.* **298** (2023), [10.1007/s11207-023-02173-y](https://doi.org/10.1007/s11207-023-02173-y).
- ³⁶F. Stefani, G. M. Horstmann, M. Klevs, G. Mamatsashvili, and T. Weier, “Rieger, Schwabe, Suess-de Vries: The sunny beats of resonance,” (2023), [arXiv:2309.00666 \[astro-ph.SR\]](https://arxiv.org/abs/2309.00666).
- ³⁷M. Seilmayer, F. Stefani, T. Gundrum, T. Weier, G. Gerbeth, M. Gellert, and G. Rüdiger, “Experimental evidence for a transient Tayler Instability in a cylindrical liquid-metal column,” *Phys. Rev. Lett.* **108**, 244501 (2012).
- ³⁸P. Jüstel, S. Röhrborn, P. Frick, V. Galindo, T. Gundrum, F. Schindler, F. Stefani, R. Stepanov, and T. Vogt, “Generating a tide-like flow in a cylindrical vessel by electromagnetic forcing,” *Phys. Fluids* **32** (2020), [10.1063/5.0015271](https://doi.org/10.1063/5.0015271).
- ³⁹P. Jüstel, S. Röhrborn, S. Eckert, V. Galindo, T. Gundrum, R. Stepanov, and F. Stefani, “Synchronizing the helicity of Rayleigh–Bénard convection by a tide-like electromagnetic forcing,” *Phys. Fluids* **34** (2022), [10.1063/5.0114035](https://doi.org/10.1063/5.0114035).
- ⁴⁰R. Mitra, M. Sieger, V. Galindo, F. Stefani, S. Eckert, and T. Wondrak, “Design of a contactless inductive flow tomography system for a large Rayleigh–Bénard convection cell,” *Flow Meas. Instrum.* (2024), (in preparation).
- ⁴¹F. Stefani and G. Gerbeth, “A contactless method for velocity reconstruction in electrically conducting fluids,” *Meas. Sci. Technol.* **11**, 758–765 (2000).
- ⁴²F. Stefani and G. Gerbeth, “On the uniqueness of velocity reconstruction in conducting fluids from measurements of induced electromagnetic fields,” *Inverse Probl.* **16**, 1–9 (2000).
- ⁴³F. Stefani, T. Gundrum, and G. Gerbeth, “Contactless inductive flow tomography,” *Phys. Rev. E* **70**, 056306 (2004).
- ⁴⁴R. Mitra, M. Sieger, V. Galindo, F. Stefani, S. Eckert, and T. Wondrak, “Flow reconstruction in a Rayleigh–Bénard convection cell with an aspect ratio 0.5 by contactless inductive flow tomography,” *Magnetohydrodynamics* **58**, 81–88 (2022).
- ⁴⁵I. Glavinić, V. Galindo, F. Stefani, S. Eckert, and T. Wondrak, “Contactless inductive flow tomography for real-time control of electromagnetic actuators in metal casting,” *Sensors* **22** (2022), [10.3390/s22114155](https://doi.org/10.3390/s22114155).
- ⁴⁶I. N. Kitiashvili, A. G. Kosovichev, N. N. Mansour, and A. A. Wray, “Realistic modeling of local dynamo processes on the sun,” *Astrophys. J.* **809**, 84 (2015).